MULTI-FREQUENCY POLINSAR SIGNATURES OF A SUBPOLAR GLACIER

Jayanti J. Sharma *, Irena Hajnsek *, Konstantinos P. Papathanassiou *
* *Microwaves and Radar Institute, German Aerospace Center 82230 Wessling, Germany*
Email: jayanti.sharma@dlr.de, irena.hajnsek@dlr.de, kostas.papathanassiou@dlr.de

ABSTRACT

In recent years there has been increased interest in using SAR to study and monitor glaciers and ice sheets for glaciological and climate change research. This paper relates the complex interferometric coherence of land ice to an extinction coefficient and ground-to-volume scattering ratio, and validates this model with airborne PolInSAR data at L- and P-band collected using DLR's E-SAR system over the Austfonna ice cap in Svalbard, Norway. Observed coherences are compared with several PolInSAR scattering models including random volume (RV), random volume under ground (RVuG), oriented volume (OV) and oriented volume under ground (OVuG). In all cases the ice volume is approximated as an infinitely thick and uniformly lossy medium.

Model predictions of interferometric coherence using estimated surface-to-volume scattering ratios and extinctions are validated against observed coherences referenced to corner reflectors deployed on the ice's surface. Measured and modelled phase centres were found to be in agreement within a few metres. The distribution of complex coherences on the unit circle suggests a possible oriented volume under ground (OVuG) scattering scenario for a significant portion of L-band PolInSAR observations in the ablation zone, although a limited observation space does not allow us to reach any firm conclusions regarding model suitability at P-band.

1 INTRODUCTION

The last decade has seen an increasing demand for accurate and wide-coverage monitoring of glaciers and ice sheets in order to measure and predict their response to global climate change and their contribution to sea level rise. This in turn requires a greater understanding of their properties including topography, velocity, melting and accumulation rates, and internal structures.

SAR (Synthetic Aperture Radar) is a powerful remote sensing tool with which to measure glaciers due to its high spatial resolution and wide coverage, and its ability to penetrate beneath the ice's surface to observe subsurface structures. However, SAR backscattering from ice remains poorly understood. The relative importance of scattering from the air/snow and snow/ice interfaces, from internal layers and structures in the firn, and from individual ice particles is unclear, as well as the dependence of the land ice radar signatures on frequency and glacier facie. Few models address the interferometric coherence as an observable, and the greatest focus to date has been on modelling single-polarisation backscattering coefficients.

Interferometric coherence magnitudes at C-band were modelled in [1] by means of ERS-1/2 data, although only a single polarisation was available, and validation was hampered by both a lack of surface reflectors (providing reference heights) and by an unknown temporal decorrelation component. First attempts at modelling PolInSAR observables at C- and L-band over ice were given in [2], although no satisfactory and physically-realistic model was found to explain the observed coherences.

The objective of this paper is to relate the complex interferometric coherence of land ice to a set of parameters and to validate this model with airborne PolInSAR data. Section 2 reviews several PolInSAR scattering models including random volume (RV), random volume under ground (RVuG), oriented volume (OV) and oriented volume under ground (OVuG) adapted to a glacier geometry. Section 3 describes the test site and experimental data. Sections 4 and 5 model coherence magnitude and complex coherence respectively, using both simulations and analysis of experimental data. Model predictions are validated using observed coherences referenced to corner reflectors deployed on the ice's surface.

2 COHERENCE MODELS FOR LAND ICE

In the following we review a few simple single- and dual-layer scattering models relating the complex interferometric coherence to geophysical ice parameters. The models are similar to the oriented volume and random volume over ground models proposed in [3]–[6], but are adapted to a glacier geometry which differs from the vegetation scenario in that:

1) At microwave wavelengths glaciers can be considered infinitely thick [1], [2].
2) Surface scattering (if significant) occurs at the top of the volume, whereas in the forest scenario the ground lies at the bottom of the forest volume [2].
3) Upon entering the ice medium the wavelength is reduced by a factor of $\sqrt{\varepsilon}$ (where ε is the permittivity) and refraction changes the incidence angle from θ to θ_r according to Snell's law.

In the following analysis, we consider models characterised by different combinations of ice properties,

namely:

- polarimetric dependency of propagation (corresponding to a random or an oriented volume)
- surface contribution (negligible or significant)

With these properties, four models can be defined in terms of their volume isotropy and surface contribution [2]:

- Random Volume model (RV)
- Oriented Volume model (OV)
- Random Volume under Ground model (RVuG)
- Oriented Volume under Ground model (OVuG)

The following sections derive a general coherence expression to represent these models, beginning with a volume-only scenario in section 2.1 and a coupled ground/volume scattering scenario in section 2.2

2.1 Coherence from an ice-volume

As in [1] we model the ice volume as a semi-infinite half-space consisting of a uniform distribution of scatterers with dielectric constant $\sqrt{\varepsilon}$. The volume extends from the surface (located at $z = 0$) downwards with radar viewing geometry given in Fig.1. The two antennae are separated by baseline B (with component $B_\perp$ perpendicular to the line-of-sight) and observe a point on the ground at incidence angle θ. As the EM wave enters the snow, it is refracted at an angle $\theta_{\rm snow}$ to the vertical, and is refracted once more to θ_r in the ice volume. The difference in look angles from each antenna is $\Delta\theta$ in air and $\Delta\theta_r$ in the volume (not shown in the diagram), and $d_{\rm snow}$ and $d_{\rm pen}$ are the snow depth and penetration depth in the ice volume, respectively. The principle InSAR

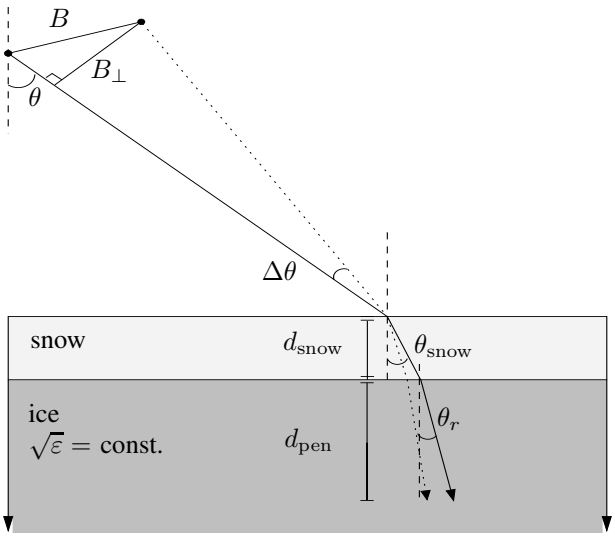

Fig. 1: InSAR geometry (not to scale) for penetration in glacier ice assuming a uniform volume with dielectric constant $\sqrt{\varepsilon}$.

observable is the complex coherence γ (see e.g. [7], [8]). Assuming that the sources of decorrelation are statistically independent [9], we can describe the total observed complex coherence as the product of several components:

$$\gamma_{\rm total} = e^{-j\phi_0} \cdot \gamma_{\rm vol} \cdot \gamma_{\rm range} \cdot \gamma_{\rm SNR}, \tag{1}$$

where ϕ_0 is the topographic phase, $\gamma_{\rm vol}$ is the volumetric decorrelation, $\gamma_{\rm range}$ is the spectral range decorrelation due to slightly different look angles between the master and slave antennae, and $\gamma_{\rm SNR}$ is the signal-to-noise ratio (SNR) decorrelation. It is assumed that there is no temporal decorrelation since the time interval between passes in the experimental data were relatively short at 15 minutes, and that any decorrelation from processing errors (e.g. coregistration, quantisation) is small relative to other sources of decorrelation.

We would like to isolate the volumetric coherence due to its sensitivity to the geophysical parameters of the glacial volume. Assuming the surface to be flat and the RCS (radar cross section) to vary only with depth within the coherence window (i.e. RCS $\sigma_v(x, y, z) = \sigma_v(z)$), we can separate the decorrelation sources in the y (range) and z (vertical) dimensions and write Eq. 1 as [1], [10]:

$$\gamma_{\rm total} = e^{-j\phi_0} \cdot \frac{\int \sigma_v(z) e^{-jk_{z\rm vol}z} dz}{\int \sigma_v(z) dz} \cdot \frac{\int |W_{\rm rng}(y)|^2 e^{-j\Delta k_y y} dy}{\int |W_{\rm rng}(y)|^2 dy} \cdot \frac{1}{1 + {\rm SNR}^{-1}}, \tag{2}$$

where $W_{\rm rng}(y)$ is the range impulse response, $\sigma_v(z)$ the volumetric RCS vertical structure function, SNR is the signal-to-noise ratio, and Δk_y and k_{zvol} are the ground range wave number difference and vertical wave number in the volume defined, respectively, as:

$$\Delta k_y = \frac{4\pi}{\lambda} \cos\theta \Delta\theta \tag{3}$$

$$k_{z\rm vol} = \frac{4\pi\sqrt{\varepsilon}}{\lambda} \frac{\Delta\theta_r}{\sin\theta_r} = k_z \sqrt{\varepsilon} \frac{\cos\theta}{\cos\theta_r}. \tag{4}$$

where $k_z = (4\pi\Delta\theta)/(\lambda \sin\theta)$ is the vertical wave number from e.g. [5]. Assuming that the volume consists of uniformly distributed and uncorrelated scattering centres, there is constant extinction such that the vertical structure function $\sigma_v(z)$ from the volumetric coherence term (first integral in Eq. 2) is an exponential:

$$\sigma_v(z) = \sigma_v^0 e^{\frac{2z\kappa_e}{\cos\theta_r}}, \tag{5}$$

where σ_v^0 is the averaged RCS per unit volume and κ_e is the extinction coefficient in units of $\rm m^{-1}$. The extinction coefficient may also be expressed in terms of the penetration depth at which the one-way backscattered power falls to $1/e$ given by [11]:

$$\kappa_e = -\cos\theta_r / d_{\rm pen}, \tag{6}$$

where the $\cos\theta_r$ factor accounts for the off-vertical travel distance of the wave within the medium.

Substitution of Eq. 5 into the volumetric coherence equation (first integral of Eq. 2), and evaluation of the integral for limits $-\infty < z < 0$ yields a complex volumetric coherence of:

$$\gamma_{\text{vol}} = \frac{1}{1 + \frac{j \cos\theta_r k_{z\text{vol}}}{2\kappa_e}}. \quad (7)$$

Volume orientation manifests itself in the coherence equation with a polarisation dependency of the extinction parameter $\kappa_e(\vec{w})$, where $\vec{w}$ is a three-component unitary complex vector defining the polarisation state.

2.2 Coherence from an ice-volume/ground scenario

We now consider a ground scattering contribution in addition to scattering from the ice volume. The surface scattering contribution is introduced by the surface-to-volume scattering intensity ratio m given by:

$$m(\vec{w}) = \frac{m_g(\vec{w})}{m_v T_{s,i}(\vec{w}) T_{i,s}(\vec{w})}, \quad (8)$$

where m_g is the ground scattering intensity, m_v the volume scattering intensity, and $T_{s,i}$ and $T_{i,s}$ the snow-ice and ice-snow transmissivities (the fraction of transmitted incident radiation). Since snow is widely assumed to be transparent at the microwave wavelengths under consideration, we assume full transmission of the signal at the air-snow interface. Note that $m(\vec{w})$ is polarisation dependent.

Let γ_z represent the coherence from a combination of volume scattering with complex coherence γ_{vol} and a surface scattering component whose strength is determined by the positive scalar m. After correction of SNR and range spectral decorrelation the complex coherence is given as [2]:

$$\gamma_z(\vec{w}) = e^{-j\phi_0} \frac{\gamma_{\text{vol}}(\kappa_e(\vec{w}), \varepsilon) + m(\vec{w}, \varepsilon)}{1 + m(\vec{w}, \varepsilon)}. \quad (9)$$

Eqn. 9 is our fundamental modelling equation with unknowns ϕ_0, $\kappa_e(\vec{w})$ and $m(\vec{w})$, and observables $\gamma_z(\vec{w})$, where one complex coherence $\gamma_z(\vec{w})$ is available for each interferometric baseline.

3 Experimental Data

3.1 Test site

The test sites lie on the island of Nordaustlandet in northeastern Svalbard, Norway (~79-80°N, 20-27°E) in the subpolar glacial regime [12]. Two sites were overflown, one near the summit of the Austfonna ice cap, the largest ice cap in the Eurasian Arctic [13], and one over the Etonbreen drainage basin, an outlet glacier of the ice cap. These sites are subsequently referred to as 'Summit' and 'Glacier', respectively. The Summit test site lies in the accumulation zone and Glacier in the ablation zone, and therefore different vertical ice structures are possible. Topography is very gentle with surface slopes of generally less than 1° at both sites, although while the surface of Summit was essentially featureless, the Glacier test site exhibited small topographic undulations.

3.2 SAR data and ground measurements

The SAR data were obtained as part of the SVALEX (SVALbard airborne EXperiment) in April 2005, a joint project of the Microwaves and Radar Systems Institute of the German Aerospace Center (DLR) and the Alfred-Wegener Institute (AWI). Single-pass X-band data at VV polarisation and repeat-pass fully-polarised L-band (1.3

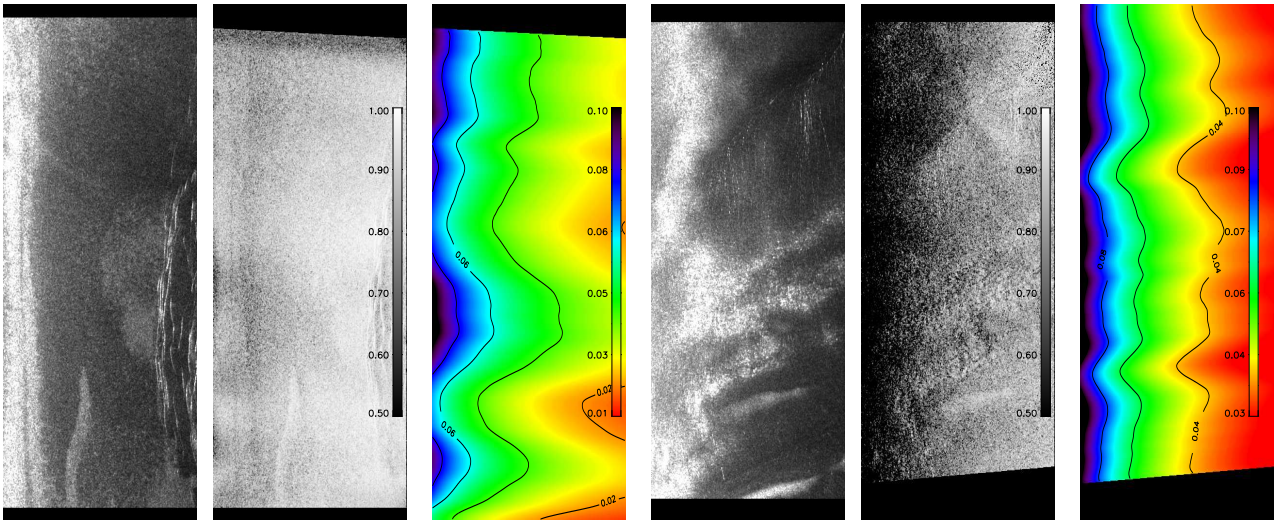

(a) $|HH|^2$ **(b)** $|\gamma_{\text{vol}}|$ **(c)** k_z **(d)** $|HH|^2$ **(e)** $|\gamma_{\text{vol}}|$ **(f)** k_z

Fig. 2: P-band Summit (a-c) and Glacier (d-f) data at HH polarisation, where coherence measures are for a 15 m baseline. Flight (azimuth) direction is from bottom to top.

GHz) and P-band (350 MHz) data were collected using DLR's E-SAR (Experimental SAR) system. Repeat-passes were flown at nominal baselines of 5, 10 and 15 m at an aircraft altitude of 5.5 km. Incidence angles varied from 25-50° and the data have a slant-range resolution of 1.5 m and an azimuth resolution of 0.67 m (L-band) and 2.0 m (P-band). This analysis concentrates on the L- and P-band fully polarimetric data. P-band intensity, coherence magnitude (after correction of γ_{SNR} and γ_{range}) and k_z images for both the Summit and Glacier test sites are shown in Fig.2.

For calibration purposes and to determine the location of the ground surface, several corner reflectors and an approximately 200-m-long wire were deployed directly on the surface of the ice. Also required for use of the model in Eq. 9 is an estimate of the dielectric permittivity ε which was computed from an empirical relation to firn density [14]. An approximate firn density of $\rho_{\mathrm{firn}} = 0.8$ g/cm^3 (the mean of a 16 m ice core extracted near the Summit area) yielded permittivity $\varepsilon = 2.8$. This value is assumed throughout for all simulations and experimental data. The angle of refraction in the volume θ_r was determined from successive application of Snell's law to a signal propagating through the air-snow and snow-ice interfaces, where a permittivity of $\varepsilon_{\mathrm{snow}} \simeq 1.7$ was assumed based on a snow density of 0.4 g/cm^3 [15], [16]. In section 4.2.1 a snow depth of 1 m is assumed based on the average depth to the previous summer ice surface from two snow pits at the test sites.

4 Modelling Coherence Magnitude

Initially we consider only the magnitude of the coherence, as in previous studies of InSAR data over land ice [1], [10]. Taking the absolute value of complex coherences in Eqs. 7 and 9 yields coherence magnitudes:

$$|\gamma_{\mathrm{vol}}(\vec{w})| = \frac{1}{\sqrt{1 + \left(\frac{\cos\theta_r k_{z\mathrm{vol}}}{2\kappa_e(\vec{w})}\right)^2}} \qquad (10)$$

and

$$|\gamma_z(\vec{w})| = \left|\frac{\gamma_{\mathrm{vol}}(\vec{w}) + m(\vec{w})}{1 + m(\vec{w})}\right|. \qquad (11)$$

Simulations of coherence magnitude and comparisons of modelled results with experimental data are given in sections 4.1 and 4.2.

4.1 Coherence magnitude model simulations

Simulations both with and without a ground contribution ($0 \leq m \leq 2$) and with varying extinction coefficients ($0.1 \leq \kappa_e \leq 0.5$ dB/m) were carried out. Little is available in the literature as to realistic values for these parameters at L- and P-band, although at C-band values on the order of $\kappa_e \approx 0.4$ dB/m (corresponding to penetration depths on the order of 20 m) have been reported in [1], [10], [14], [17] for dry firn and snow

Fig.3(a) graphs the volume only scenario ($m = 0$) from Eq. 10 for various extinction coefficients κ_e and varying k_z (Eq. 4) from 0 to 0.5. Low coherence magnitudes are seen for increasing k_z, although larger extinctions result in a shallower penetration depth, and thus less volume decorrelation resulting in higher coherence magnitudes. In Fig.3(b) the extinction is fixed at $\kappa_e = 0.3$ dB/m and the coherence magnitude as a function of k_z is plotted for several ground-to-volume scattering ratios m. It is seen that an increasing ground contribution raises coherence magnitudes, with this effect being particularly pronounced at higher k_z values.

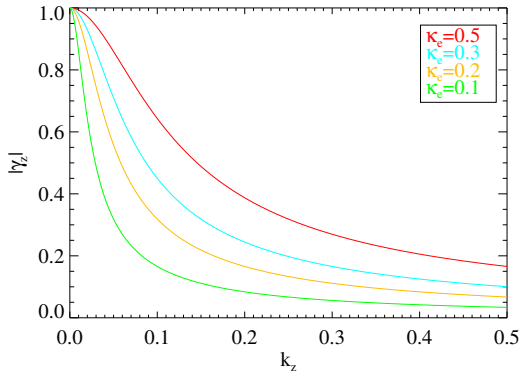

(a) Coherence magnitude $|\gamma_z|$ versus k_z for varying extinction $0.1 \leq \kappa_e \leq 0.5$ dB/m and no ground contribution $m = 0$.

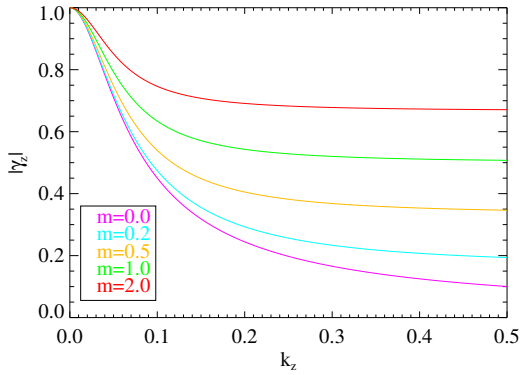

(b) Coherence magnitude $|\gamma_z|$ versus k_z for varying ground contribution $0 \leq m \leq 2$ and constant extinction $\kappa_e = 0.3$ dB/m.

Fig. 3: Simulated coherence magnitudes for (a) volume with varying extinction coefficients κ_e and (b) volume with ground contribution for various surface-to-volume scattering ratios m.

4.2 Coherence magnitude model applied to experimental data

We now fit observed coherences magnitudes from experimental data to the model described by Eq. 11. As in the simulations, we plot $|\gamma_z|$ versus $|k_z|$ for a single azimuth angle. A single θ is plotted in order to obtain a unique mapping between $|\gamma_z|$ and $|k_z|$, and absolute k_z values are used since at the smaller 5 m baselines the aircraft flight-tracks sometimes crossed one another. Variation

in k_z is obtained from baseline-diversity (nominal 5, 10 and 15 m baselines) as well as from the variable flight tracks. L-band HV coherences at all baselines for an azimuth strip along $\theta = 35°$ at the Summit and Glacier test sites are shown in Fig.4. Various combinations of baselines were formed from four parallel flight tracks and are labelled e.g. 'B=5.0' for a nominal 5 m baseline between tracks 0 and 1, and 'B=5.1' for a nominal 5 m baseline between tracks 1 and 2.

Non-linear least-squares (applying the Levenberg-Marquardt technique) is used to determine the best-fit κ_e and m parameters of the model in Eq. 11 to the data. The solution is constrained such that $\kappa_e \geq 0$ and $m \geq 0$. Modelled $|\gamma_z|$ derived using the best-fit parameters to Eq. 11 are shown in solid black in Fig.4. Estimated κ_e and m parameters at $\theta = 35°$ at different polarisations and test sites, as well as the R^2 values (coefficients of determination) for L-band are given in Table 1. Unfortunately there was insufficient k_z diversity in the P-band data to draw any meaningful conclusions regarding the model suitability. This low k_z diversity is seen in Fig.2), in which k_z varied from only 0 to a maximum of 0.05 at $\theta = 35°$.

TABLE 1: Best-fit extinctions (κ_e, dB/m) and ground-to-volume scattering ratios (m) to Eq. 11 at $\theta = 35°$, as well as R^2 values of the fit.

	Summit			Glacier		
	HH	VV	HV	HH	VV	HV
κ_e	0.59	0.61	0.40	0.51	0.58	0.43
m	1.1	0.9	0.2	0.0	0.0	0.0
R^2	0.91	0.92	0.96	0.83	0.83	0.80

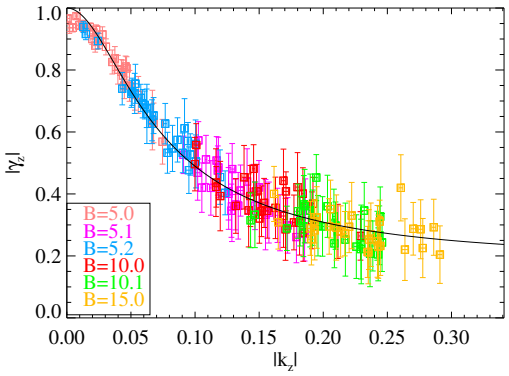

(a) Summit results with best-fit $m = 0.2$, $\kappa_e = 0.40$ dB/m.

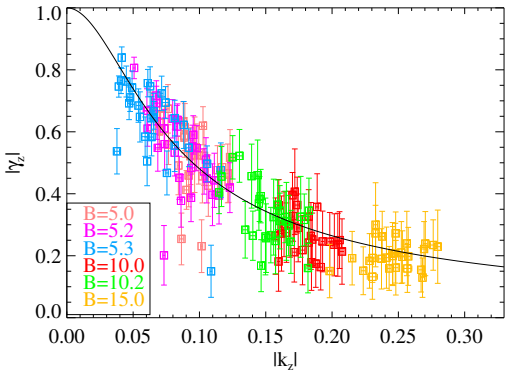

(b) Glacier results with best-fit $m = 0.0$, $\kappa_e = 0.43$ dB/m.

Fig. 4: L-band HV coherence magnitudes and standard deviations along azimuth line $\theta = 35°$. The best-fit model (Eq. 11) to the data is shown in solid black.

In general there is a good fit of the model to the data with R^2 values greater than 0.9 at Summit. As seen from the backscattering images from Fig.2, the Glacier test site is much more inhomogeneous than Summit, resulting in increased scatter in the coherences and lower R^2 values, although the model still provides a reasonable fit. The ground contribution at Glacier from the model is negligible, which may be due to a smoother snow-ice interface (resulting in increased specular reflection) as it is part of the ablation zone whereas Summit lies in the accumulation zone. L-band extinction coefficients were on the order of 0.4-0.6 dB/m which are similar to results at C-band from Greenland and Antarctica [1], [10], [14], [17] measured under different ice conditions as the Svalbard data. It is possible that structures in the ice and increased densities at shallower depths in Svalbard glaciers compared with central regions of the large ice sheets (which undergo less melt metamorphosis) may explain the relatively high extinction coefficients at low frequencies.

4.2.1 Validation with ground reflectors: The coherence magnitude model may also be validated by comparing modelled phase centres to phase measurements referenced using ground reflectors deployed on the ice. For L-band, pixels within ± 80 m of a corner reflector (CR) at the Glacier test site were used in the least-squares fit giving a κ_e of 0.33 and 0.35 dB/m at HH and VV respectively, and $m = 0$ for both polarisations (only co-pol channels were considered since the CR is not visible at HV). As there is no ground contribution we convert κ_e to penetration depth d_{pen} by using Eq. 6, and adjust the depth to correspond to the 50% two-way power (i.e. phase centre) where d_{model} (50%, 2-way power) $= d_{\text{pen}} \ln 0.5/2$.

The phase centres of the complex coherences were computed by subtracting the mean coherence phase evaluated in an area surrounding the CR by the interferometric phase at the CR, followed by division by $k_{z\text{vol}}$ to give $d_{\Delta\phi}$. In the previous step a phase bias from the overlying snow cover was removed to bring the reflectors down to the snow-ice rather than air-snow interface.

At P-band a wire rather than a CR was available, and due to its horizontal orientation it was only visible at HH. As mentioned above, there was insufficient k_z diversity in the P-band data to apply a least-squares fit and therefore m was set to zero for inversion of Eq. 11, yielding κ_e and thus d_{model}. The modelled depths from each baseline were averaged together to obtain a single value. The phase centre was determined using the same procedure as at L-band, where the brightest point on the wire (with the highest backscatter) was used for reference. One problem with the wire is that it had a width of only a few cm, such that a given resolution cell contains contributions from the ice as well as the wire, and thus the measured phase centre may be biased.

The modelled and measured phase centres at L- and P-band for the Glacier test site are shown in Table 2, where the measured phase centres are the average of $d_{\Delta\phi}$ values at all baselines. There is very good agreement at L-band with a phase centre of ∼-8 m, although as expected at P-band, the measured phase centre of -15 m is shallower than the modelled value of -17m, likely for the reasons explained above.

TABLE 2: Phase centres computed from the coherence magnitude model (d_{model}, corresponding to 50%, 2-way power) and from phase differences to ground reflectors $d_{\Delta\phi}$ at the Glacier test site.

	L-band		P-band
	HH	VV	HH
d_{model} [m]	-8.4±1.5	-7.9±1.3	-17.0±5.0
$d_{\Delta\phi}$ [m]	-8.2±1.8	-7.3±1.8	-14.8±3.3

5 Modelling Complex Coherence

Although the fit between the observed and predicted coherence magnitudes in the previous section were quite good, this modelling strategy can be problematic for several reasons. Firstly, it requires large baseline diversity and homogeneous terrain, such that values over a range of azimuth pixels can be described by the same m and κ_e parameters. As well, coherence magnitudes can be very sensitive to additional uncorrected sources of decorrelation in the data. For these reasons we look to the additional information provided by complex coherences, available on a sample-by-sample basis without an assumption of homogeneity.

5.1 Complex coherence simulations

A useful visualisation of complex coherence is on the unit circle, where the x-y axes are the real and imaginary parts of the coherence, the distance from the origin represents coherent magnitude and the angle from 0° is the interferometric phase. A theoretical ground point (e.g. corner reflector) with arbitrarily chosen topographic phase $\phi_0 = 0$ is located at $1 + 0j$. To understand the complex coherences predicted from the various models in section 2 we plot theoretical curves on the unit circle corresponding to various extinctions and ground-to-volume scattering ratios. The simulated coherences for a random volume under ground (RVuG) and an oriented volume under ground (OVuG) with k_z varied from 0 to 0.5 are shown in Figs. 5(a) and 5(b), where the models reduce to the random volume (RV) and oriented volume (OV) scenarios for the $m = 0$ curves. The difference between a RV and an OV is that in an oriented volume the extinction is polarisation-dependent.

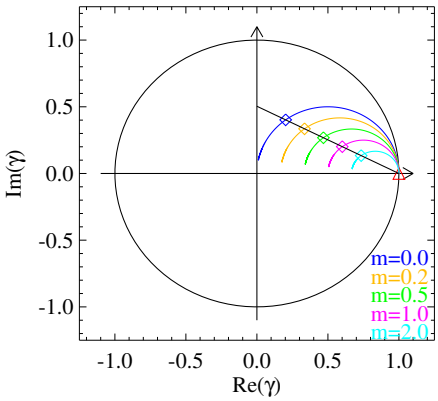

(a) Complex coherences on the unit circle for a RVuG scenario with varying ground contributions $0 \leq m \leq 2$ and fixed extinction $\kappa_e = 0.3$ dB/m.

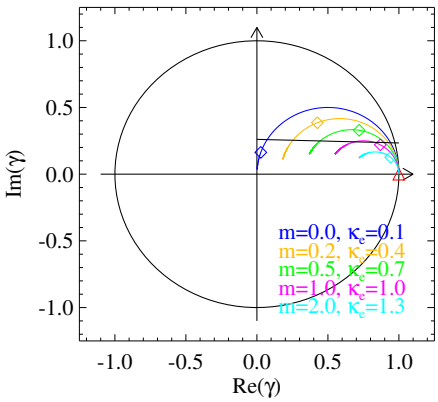

(b) Complex coherences on the unit circle for an OVuG scenario with both varying extinctions $0.1 \leq \kappa_e \leq 1.3$ dB/m and ground contributions $0 \leq m \leq 2$.

Fig. 5: Simulated complex coherences for a (a) RVuG scenario (b) OVuG scenario. The red triangle represents a theoretical ground point at $1+0j$, and the diamonds are coherence values for $k_z = 0.1$.

In the case of a RV or an OV all coherences lie on a semi-circle centred at $0.5 + 0j$ with radius 0.5. The addition of a non-zero ground contribution (applicable to RVuG and OVuG models) increases coherence magnitudes, shifting the coherence curves closer to the

theoretical ground point. To generate RVuG coherences, the extinction κ_e is fixed for all polarisations, although $m(\vec{w})$ is allowed to vary with polarisation. One interesting geometrical property of RVuG coherences is that they form a line passing through the ground point $e^{j\phi_0}$, illustrated in Fig.5(a). However, in an OVuG scenario, where both $\kappa_e(\vec{w})$ and $m(\vec{w})$ vary with polarisation, the coherences do not lie on a line. If a best-fit line through the coherences is drawn (as a potential test for an RVuG scenario) it is seen from Fig.5(b) that it does not pass through the ground point, and as opposed to the RVuG case such a line has no physical meaning.

5.2 Complex coherence models applied to experimental data

Observed values of complex coherence referenced to ground reflectors are compared against the coherence models described in the previous section. Characteristics such as the location of the coherences in relation to the ground topography point, and the spread and variation in coherence amplitude and phase may give an indication of an appropriate coherence model to interpret the obtained PolInSAR signatures.

The interferometric reflector phase (taken as the average of the 2 co-pol phases at L-band, and as the HH phase at P-band) was subtracted from the complex coherences of pixels lying near the reflectors in order to place the surface point at $1 + 0j$. As described in section 4.2.1, the snow phase bias is removed from the data and $k_{z\mathrm{vol}}$ and θ_r values take into account propagation through an overlying winter snow cover. Examples showing both coherences in the linear polarisation basis and the coherence boundary region (see [18]) are provided in Fig.6 for one L-band and one P-band pixel. The ground reflectors are represented by triangles, where their coherences are computed using a smaller [3x3] coherence window than for the ice data. This spatial averaging introduces coherence magnitudes slightly less than unity and small phase offsets from the interferogram value at the peak corner/wire pixel, but they serve as a useful reference for the other coherences.

We now compare each of the four models to the coherences from the experimental data at a single k_z value. In a RV scenario, all coherences collapse or cluster at a single point since there is no polarisation-dependency on extinction. However, in the experimental data from Fig.6 there is a clear spread of coherences with polarisation at both frequencies. In the case of an OV the coherences should lie on or near a semi-circle with radius 0.5 passing through the origin and the ground point. This model also seems not fit the data, with γ_{HH} at L-band and γ_{HV} at P-band lying distinctly below such a semicircle. If an RVuG model were to apply, the major axis of the coherency boundary ellipse should pass through the ground point, but it is evident from

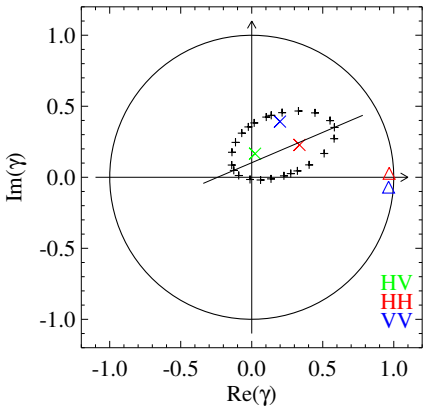

(a) L-band Glacier near CR, B=5 m, $k_z = 0.09$.

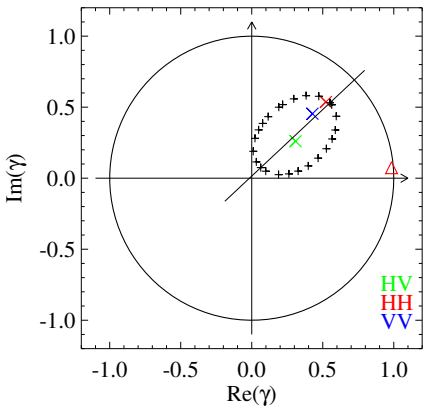

(b) P-band Glacier near wire, B=15 m, $k_z = 0.05$

Fig. 6: Complex coherences from L- and P-band Glacier data referenced to ground reflectors, whose coherences are given by the triangles. Polarisations in the linear basis and the coherence boundary regions are plotted. Also indicated are the major axes of the coherence boundary ellipses.

both plots that this is not the case. This leaves us with the most general OVuG model as a possible candidate.

For the OVuG model to apply - as we have defined it (i.e. assuming an infinite and uniform volume) - the coherence phases must lie between 0 and 90° and the coherence point must fall within the semicircle defined by $0.5^2 = \mathrm{Re}\{\gamma_z\}^2 + \mathrm{Im}\{\gamma_z\}^2$ for $\mathrm{Re}\{\gamma_z\} \geq 0$ and $\mathrm{Im}\{\gamma_z\} \geq 0$, as demonstrated in the simulations from Fig.5. For the L-band example provided in Fig.6(a) the three linear polarisations and nearly the entire coherence region lies within this semicircle, although for some neighbouring pixels (not shown), the coherences lie predominantly outside these bounds. Residual decorrelation and noise effects could shift coherences and artificially expand the boundary ellipse, although it is assumed that these effects have been compensated. At L-band between

30-50% of pixels in a 60mx60m area surrounding the corner satisfied the OVuG criterion for the linear polarisation basis (results varied with baseline), although at P-band only 5% of pixels met the criterion. Thus, while OVuG may be useful in describing a portion of ablation zone land ice PolInSAR observables at L-band, it is unable to explain all observed coherences, particularly at P-band. However, the inconsistency between model and data could lie in a non-optimally sampled observation space, i.e. with P-band k_z values outside the region of sensitivity to vertical structure, and thus at this time we are unable to draw any firm conclusions regarding model suitability.

6 SUMMARY

In this paper we have adapted single- and two-layer PolInSAR models to a glacier geometry. It was found that modelled coherence magnitudes provide a reasonable match to experimental data at multiple polarisations at L-band, although there was insufficient k_z diversity at P-band to draw conclusions regarding model suitability. Although useful for verifying the validity of the underlying coherence model, this technique is generally unsuitable for inversion due to the requirement of homogeneity in azimuth and high k_z diversity, and the method is sensitive to decorrelation effects.

The data exhibit polarimetric interferometric effects in the sense that the amplitude as well as the phase of the complex coherence depends on the polarisation. Complex coherences were examined and their locations were referenced to ground reflectors to evaluate the suitability of the proposed coherence models. Although modelling of PolInSAR data for land ice is still at a relatively early stage of development, initial results indicate a possible Oriented Volume under Ground (OVuG) scenario for L-band data from the ablation zone, although not all coherence data are consistent with such a model and not all lie within the required semicircle assuming a uniform infinite volume. As demonstrated with modelling of coherence magnitude, the interferometric coherence behaviour can be described with a simple two-layer model, although a polarimetric interpretation of the data has not yet been established. Future work will focus on investigating the fit of the models at the Summit test site and exploring other possible representations of the vertical structure variation in land ice and the resulting complex coherence observables.

ACKNOWLEDGEMENTS

The authors would like to extend their thanks to their partners in the SVALEX campaign including colleagues at the Alfred-Wegner Institute (AWI), the University of Oslo (UiO) and the Norwegian Polar Institute (NPI). This work has been funded by the Microwaves and Radar Systems Institute of the German Aerospace Center (DLR) and the DAAD (German Academic Exchange Service).

REFERENCES

[1] W. Hoen, "A correlation-based approach to modeling interferometric radar observations of the Greenland ice sheet," Ph.D. dissertation, Department of Applied Physics, Stanford University, March 2001.

[2] J. Dall, K. P. Papathanassiou, and H. Skriver, "Polarimetric SAR interferometry applied to land ice: modeling," in *Proc. of European Synthetic Aperture Radar Conference (EUSAR)*, Ulm, Germany, May 2004, pp. 247–250.

[3] R. N. Treuhaft and P. R. Siqueira, "Vertical structure of vegetated land surfaces from interferometric and polarimetric radar," *Radio Science*, vol. 35, no. 1, pp. 141–177, January-February 2000.

[4] R. N. Treuhaft and S. R. Cloude, "The structure of oriented vegetation from polarimetric interferometry," *IEEE Trans. Geosci. Remote Sens.*, vol. 37, no. 5, pp. 2620–2624, September 1999.

[5] K. P. Papathanassiou and S. R. Cloude, "Single-baseline polarimetric SAR interferometry," *IEEE Trans. Geosci. Remote Sens.*, vol. 39, no. 11, pp. 2352–2363, November 2001.

[6] S. R. Cloude and K. P. Papathanassiou, "Three-stage inversion process for polarimetric SAR interferometry," *IEE Proc.-Radar Sonar Navig.*, vol. 150, no. 3, pp. 125–134, June 2003.

[7] R. Bamler and P. Hartl, "Synthetic aperture radar interferometry," *IEEE Transactions on Geoscience and Remote Sensing, Inverse Problems*, vol. 14, pp. R1–R54, May 1998.

[8] P. Rosen, S. Hensley, I. Joughin, F. Li, S. Madsen, E. Rodriguez, and R. Goldstein, "Synthetic aperture radar interferometry," *Proceedings of the International IEEE*, vol. 88, no. 3, pp. 333–382, March 2000.

[9] G. Krieger, K. P. Papathanassiou, and S. R. Cloude, "Spaceborne polarimetric SAR interferometry: Performance analysis and mission concepts," *EURASIP journal on Applied Signal Processing*, vol. 20, pp. 3272–3292, 2005.

[10] E. W. Hoen and H. Zebker, "Penetration depths inferred from interferometric volume decorrelation observed over the greenland ice sheet," *IEEE Trans. Geosci. Remote Sens.*, vol. 38, no. 6, pp. 2572–2583, November 2000.

[11] F. T. Ulaby, R. K. Moore, and A. K. Fung, *Microwave Remote Sensing, Active and Passive, Volume II: Radar Remote Sensing and Surface Scattering and Emission Theory*. Reading, MA: Addison-Wesley, 1982.

[12] J. O. Hagen, J. Kohler, K. Melvold, and J.-G. Winther, "Glaciers in Svalbard: mass balance, runoff and freshwater flux," *Polar Res.*, vol. 22, no. 2, pp. 145–159, 2003.

[13] J. Bamber, S. Ekholm, and W. B. Krabill, "Anomalous recent growth of part of a large arctic ice cap: Austfonna, Svalbard," *Geophys. Res. Lett.*, vol. 31, no. 12, pp. 1–4, 2004.

[14] C. Mätzler, "Applications of the interaction of microwaves with natural snow cover," *Remote sensing reviews*, vol. 2, pp. 259–387, 1987.

[15] J. Pinglot, J. Hagen, K. Melvold, T. Eiken, and C. Vincent, "A mean net accumulation pattern derived from radioactive layers and radar soundings on Austfonna, Nordaustlandet, Svalbard," *J. Glaciol.*, vol. 47, no. 159, pp. 555–566, 2001.

[16] A. Taurisano, J. Kohler, J. O. Hagen, T. Eiken, and E. Loe, "Cryosat calibration and validation on Austfonna, Svalbard, ESA PRODEX contract with NPI: Final report," Norwegian Polar Institute (NPI) and University of Oslo (UiO), 28 February 2005.

[17] H. Rott, K. Sturm, and H. Miller, "Active and passive microwave signatures of Antarctic firn by means of field measurements and satellite data," *Ann. Glaciol.*, vol. 17, pp. 337–343, 1993.

[18] T. Flynn, M. Tabb, and R. Carande, "Coherence region shape extraction for vegetation parameter estimation in polarimetric SAR interferometry," in *Proc. of the IEEE International Geoscience and Remote Sensing Symposium (IGARSS'02)*, 24-28 June 2002.